

GT2021-59664

## HIGH EFFICIENCY WIND TURBINE USING CO-FLOW JET ACTIVE FLOW CONTROL

Kewei Xu\*

Gecheng Zha†

Department of Mechanical and Aerospace Engineering

University of Miami

Coral Gables, Florida 33124

Emails: kxx50@miami.edu , gzha@miami.edu

### ABSTRACT

This paper applies Co-flow Jet (CFJ) active flow control airfoil to a NREL horizontal axis wind turbine for power output improvement. CFJ is a zero-net-mass-flux active flow control method that dramatically increases airfoil lift coefficient and suppresses flow separation at a low energy expenditure. The 3D Reynolds Averaged Navier-Stokes (RANS) equations with one-equation Spalart-Allmaras (SA) turbulence model are solved to simulate the 3D flows of the wind turbines. The baseline wind turbine is the NREL 10.06m diameter phase VI wind turbine and is modified to a CFJ blade by implementing CFJ along the span. The baseline wind turbine performance is validated with the experiment at three wind speeds, 7m/s, 15m/s, and 25m/s. The predicted blade surface pressure distributions and power output agree well with the experimental measurements. The study indicates that the CFJ can enhance the power output at the condition where angle of attack is increased to the level that conventional wind turbine is stalled. At the speed of 7m/s that the NREL turbine is designed to achieve the optimum efficiency at the pitch angle of 3°, the CFJ turbine does not increase the power output. When the pitch angle is reduced by 13° to -10°, the baseline wind turbine is stalled and generates negative power output at 7m/s. But the CFJ wind turbine increases the power output by 12.3% assuming CFJ fan efficiency of 80% at the same wind speed. This is an effective method to extract more power from the wind at all speeds. It is particularly useful at low speeds to decrease cut-in

speed and increase power output without exceeding the structure limit. At the freestream velocity of 15m/s and the CFJ momentum coefficient  $C_\mu$  of 0.23, the net power output is increased by 207.7% assuming the CFJ fan efficiency of 80%, compared to the baseline wind turbine due to the removal of flow separation. The CFJ wind turbine appears to open a door to a new area of wind turbine efficiency improvement and adaptive control for optimal loading.

### NOMENCLATURE

AFC	Active flow control
C	Chord
CFJ	Co-flow Jet
$C_\mu$	Momentum coefficient
$F_{zcfj}$	Jet reactionary force in torque direction
$F_{xcfj}$	Jet reactionary force in thrust direction
$H_t$	Total enthalpy
NREL	National Renewable Energy laboratory
MC	Micro-compressor
$\dot{m}$	Mass flow rate (kg/s)
$\bar{m}$	Normalized mass flow rate, $\dot{m}/\rho V_\infty A_{ref}$
TE	Trailing edge
LE	Leading edge
$P_c$	Power coefficient of CFJ
$P_{CFJ}$	Power consumed by CFJ
$P_{Wb}$	Baseline wind turbine power generation
$P_{Wc}$	CFJ wind turbine power generation

\*Ph.D. Candidate

†Professor, ASME Fellow

$P_{net}$	Net power generation improvement
$U_{\infty}$	Freestream wind speed
RPM	Round per minute
$R'$	Surface integral of pressure and shear stress
$V_{\infty}$	Freestream velocity
$V_j$	Jet velocity in rotating frame
$\bar{V}_j$	Normalized jet velocity, $V_j/U_{\infty}$
W	Watt, unit of power
ZNMF	Zero-net mass-flux
$\Gamma$	Total pressure ratio
$\eta$	Isentropic efficiency
$\theta$	Angle between CFJ slot's surface and a line normal to the airfoil chord

### Subscript

j	Jet
t	Total
1	Injection slot location
2	Suction slot location
$\infty$	Freestream values

## INTRODUCTION

Wind energy is the fastest growing energy sector due to its sustainability, renewability and low emission. Therefore, wind turbines, the machinery to extract wind energy, have been widely studied. The most important aerodynamic measure of merit of wind turbines is their power output, not at the high speed greater than the rated speed, but at the speed lower than the rated speed. When the speed is very high, the power output of a wind turbine needs to be limited to avoid the failure of the wind turbine structure and the electric generator system.

At low speed, the structure limit is not an issue and it is desirable to increase the power. Typically, a turbine is designed to have an optimum efficiency at a certain ratio of the tip speed to the freestream flow speed. When the freestream velocity is greater or smaller than that, the efficiency will drop and may be compensated by varying the pitch angle or the rotational speed. At a low speed, the way to increase the power output is to increase the aerodynamic lift coefficient and the ratio of lift to drag by increasing the angle of attack (AoA). However, the AoA is limited to avoid flow separation or blade stall. A novel aerodynamic design method that can increase the lift coefficient and the ratio of lift to drag without stalling the blade is appealing. This is the motivation of the present study.

The other important issue for wind turbine aerodynamic design is to minimize the dynamic loading due to flow separation to have long life span. A major challenge of wind turbines is the randomness nature of wind. During operation, wind direction and velocity magnitude vary constantly, which alternates flows between being separated and attached on wind turbine blades.

This fluctuation, limits the power output and exerts a periodic load on wind turbines, which reduces their operation lifespan. To increase wind turbine power output and mitigate flow fluctuation, passive and active flow control methods have been implemented on wind turbine blades.

For the passive flow control, the effects of tubercles on wind turbine performance are analyzed in [1–4]. The reduction of stall severity is achieved by using sinusoidal tubercles leading edge, which mitigates the periodic loading [3]. It is also observed that the power output of wavy blades is enhanced with the increasing of wave length [3,4]. However, tubercle leading edge decreases the power output at low wind speed due to early boundary layer separation [3,4]. Vortex generators (VGs) as a passive flow control are also commonly used on wind turbine for separation control. An increase of the stall angle is achieved by optimizing the distance between adjacent VGs [5]. Double VGs arrangements present a further performance improvement on S809 wind turbine airfoil [6]. However, drag penalty is also very sensitive to VGs. Gao et al. find that increasing VG height and length may lead to a negative effects on drag [7].

As an active flow control (AFC) with blowing jet, Air Jet Vortex Generators (AJVG) controls flow separation using the similar mechanism as vane VGs but has a more rapid respond to dynamic stall [8]. Cerretelli et al. [9] implement blowing sweeping jet on a wind turbine airfoil and achieve 10% to over 60% improvement in relative lift coefficient ( $C_L$ ) at various Reynolds number. A substantially reduced thickness of boundary layer is observed on the suction surface. However, both the AJVG [8] and sweeping jets [9] do not address how to provide the required mass flow for blowing as well as their required power that will offset the gain of the wind turbine power output.

Synthetic jet produced by the periodic motion of a piston or diaphragm is a zero-net mass-flux (ZNMF) flow control method, which does not require external flow source. It is studied numerically [10,11] and experimentally [12,13] to enhance wind turbine performance. Tran et al. [10] find that the synthetic-jet based control is able to significantly suppress the flow separation for a pitching S809 wind turbine airfoil, which reduces hysteresis by up to 73% [10]. Yen et al. [13] demonstrate that synthetic jet actuation is effective to suppress dynamic stall, which could be employed to enhance the performance of low blade tip speed ratio wind turbine.

Overall, for the various flow control methods in wind turbines, the passive flow control is more straightforward to be implemented but has limited control effectiveness. Active flow controls have higher control authority and are more effective. However, methods mentioned above are not well addressed for their energy expenditure.

The recently developed Co-flow Jet (CFJ) flow control is a ZNMF active flow control that is able to dramatically enhance the airfoil performance [14–20]. As shown in Fig. 1, a CFJ airfoil withdraws a small amount of mass flow from trailing edge,

pressurizes it by the fans, and injects the flow at leading edge tangential to the mainstream. It is demonstrated numerically and experimentally that CFJ achieves radical lift augmentation, drag reduction and stall angle of attack increase [14–20]. Lefebvre and Zha [21] implement CFJ on a pitching airfoil and basically remove its hysteresis. Xu and Zha [22] apply CFJ to S809 wind turbine airfoil and achieved an optimal configuration of CFJ-S809 airfoil with significant improvement of  $C_L$  and aerodynamic efficiency ( $C_L/C_D$ ). The purpose of this paper is to study the wind turbine energy efficiency improvement by using co-flow jet active flow control.

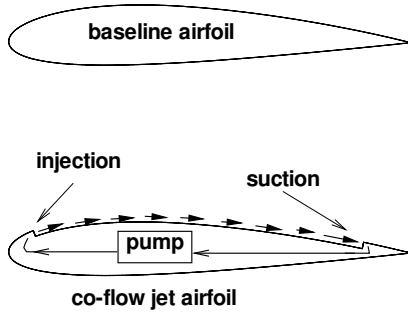


**FIGURE 1:** Schematics of the CFJ airfoil with embedded micro-compressor

## THE CO-FLOW JET PARAMETERS

To facilitate the description of CFJ wind turbine performance, several important parameters are given below.

### Jet Momentum Coefficient

The injection jet momentum coefficient  $C_\mu$  is used to describe the CFJ strength as:

$$C_\mu = \frac{\dot{m}V_j}{\frac{1}{2}\rho_\infty V_\infty^2 A_{ref}} \quad (1)$$

where  $\dot{m}$  is the injection mass flow,  $V_j$  is the mass-averaged injection relative velocity along the span,  $\rho_\infty$  denotes the free stream density, and  $A_{ref}$  is the reference area defined as the platform area of the wind turbine,  $V_\infty$  is the relative velocity at 70% span defined by Eq. (2). It combines the freestream velocity ( $U_\infty$ ) with turbine rotational velocity ( $\omega R$ ). Since the rotational velocity

varies along the span, the velocity at  $0.7R$  is taken as the averaged value.

$$V_\infty = \sqrt{U_\infty^2 + (0.7\omega R)^2} \quad (2)$$

### Power Coefficient

The CFJ power required is determined by the total enthalpy rise in the turbine rotating frame from the suction duct outlet to the injection duct inlet [15]. The total enthalpy rise can be achieved by the embedded micro-compressors. The power required by the CFJ can be expressed as:

$$P = \frac{\dot{m}H_{t2}}{\eta} (\Gamma^{\frac{\gamma-1}{\gamma}} - 1) \quad (3)$$

where,  $\dot{m}$  is the CFJ mass flow rate,  $H_{t2}$  is the total enthalpy at the suction slot,  $\Gamma$  is the total pressure ratio between the injection and suction in the turbine rotating frame, and  $\eta$  is the pumping system efficiency. For the CFJ wind turbine, the  $\dot{m}$ ,  $H_{t2}$  and  $\Gamma$  are calculated in the rotational frame of reference using relative properties.

Eq. (3) indicates that the power required by the CFJ is linearly determined by the mass flow rate and exponentially by the total pressure ratio. This relationship in fact applies to all the active flow controls based on fluidic actuators. The power coefficient is defined as:

$$P_c = \frac{P}{\frac{1}{2}\rho_\infty V_\infty^3 A_{ref}} \quad (4)$$

where  $P$  is the CFJ required power defined in Eq. (3).

## GOVERNING EQUATIONS

The governing equations are the Navier-Stokes equations in rotating frame with the effects of Coriolis force ( $2\omega \times \mathbf{V}$ ) and centrifugal force ( $\omega \times \omega \times \mathbf{r}$ ). The normalized Reynolds Averaged Navier-Stokes governing equations with Spalart–Allmaras one-equation turbulent model [24] in generalized coordinates are given by:

$$\frac{\partial \mathbf{Q}}{\partial t} + \frac{\partial \mathbf{E}}{\partial \xi} + \frac{\partial \mathbf{F}}{\partial \eta} + \frac{\partial \mathbf{G}}{\partial \zeta} = \frac{1}{Re} \left[ \frac{\partial \mathbf{R}}{\partial \xi} + \frac{\partial \mathbf{S}}{\partial \eta} + \frac{\partial \mathbf{T}}{\partial \zeta} \right] + \mathbf{D} \quad (5)$$

where  $Re$  is the Reynolds number. The conservative variable vector  $\mathbf{Q}$ , inviscid flux  $\mathbf{E}$ , viscous flux vector  $\mathbf{R}$  and source term  $\mathbf{D}$  are

expressed as follows, and the rest can be expressed following the symmetric rule.

$$\mathbf{Q} = \frac{1}{J} \begin{bmatrix} \rho \\ \rho u \\ \rho v \\ \rho w \\ \rho e \\ \rho \hat{v} \end{bmatrix} \quad (6)$$

$$\mathbf{E} = \frac{1}{J} \begin{bmatrix} \rho U \\ \rho u U + p \xi_x \\ \rho v U + p \xi_y \\ \rho w U + p \xi_z \\ (\rho e + p) U \\ \rho \hat{v} U \end{bmatrix} \quad (7)$$

$$\mathbf{R} = \frac{1}{J} \begin{bmatrix} 0 \\ \tau_{xi} \xi_i \\ \tau_{yi} \xi_i \\ \tau_{zi} \xi_i \\ (u_j \tau_{ij} - q_i) \xi_i \\ \frac{\rho}{\sigma} (\mathbf{v} + \hat{\mathbf{v}}) \frac{\partial \hat{\mathbf{v}}}{\partial x_i} \xi_i \end{bmatrix} \quad (8)$$

$$\mathbf{D} = \frac{1}{J} \begin{bmatrix} 0 \\ 0 \\ \rho R_0^2 y + 2\rho R_0 w \\ \rho R_0^2 z - 2\rho R_0 v \\ 0 \\ S_v \end{bmatrix} \quad (9)$$

where  $R_0$  is the Rossby number defined as  $(\omega L_\infty)/U_\infty$ .  $\omega$  is the angular velocity of the rotor rotation,  $L_\infty$  is the reference length and  $U_\infty$  is the freestream velocity. The normalized equation of state as a constitutive equation relating density to pressure and temperature is expressed in the rotating frame as

$$\rho e = \frac{p}{\gamma - 1} + \frac{1}{2} \rho (u^2 + v^2 + w^2) - \frac{1}{2} \rho r^2 R_0^2 \quad (10)$$

The  $S_v$  in Eq. (11) is the source term for the S-A model,

$$S_v = \rho c_{b1} (1 - f_{t2}) \tilde{S} \tilde{v} + \frac{1}{Re} \left[ -\rho \left( c_{w1} f_w - \frac{c_{b1}}{\kappa^2} f_{t2} \right) \left( \frac{\tilde{v}}{d} \right)^2 + \frac{\rho}{\sigma} c_{b2} (\nabla \tilde{v})^2 - \frac{1}{\sigma} (\mathbf{v} + \tilde{\mathbf{v}}) \nabla \tilde{\mathbf{v}} \bullet \nabla \rho \right] + Re \left[ \rho f_{t1} (\Delta q)^2 \right] \quad (11)$$

Other auxiliary relations and coefficients for the S-A turbulence model can be found in [24, 25].

## NUMERICAL METHODS

The in-house high order accuracy CFD code Flow-Acoustics-Structure Interaction Package (FASIP) is used to conduct the numerical simulation. The 3D Reynolds Averaged Navier-Stokes (RANS) equations with one-equation Spalart-Allmaras [24] turbulence model described above are solved. A 3rd order MUSCL scheme for the inviscid flux [26–28] and a 2nd order central differencing for the viscous terms are employed to discretize the Navier-Stokes equations. The low diffusion Roe flux difference scheme is used to evaluate the inviscid fluxes. Implicit time marching method using Gauss-Seidel line relaxation is used to achieve a fast convergence rate [29]. Parallel computing is implemented to save wall clock simulation time [30]. The FASIP code is intensively validated for CFJ flow control simulations [15–17, 31–37] and turbomachinery multi-stage flows [38, 39].

## THE BASELINE NREL PHASE VI ROTOR

The present study uses the Phase VI wind turbine rotor from the National Renewable Energy Laboratory (NREL) [40]. The wind turbine has two blades and the blade geometry is shown in Fig. 2, which is 5.029 meter in radius ( $R$ ) and stacked using S809 airfoil along the span. More details regarding blade geometry and wind tunnel testing can be found in [40].

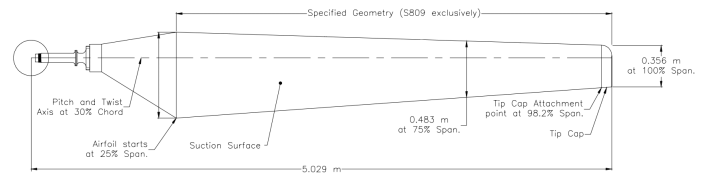


**FIGURE 2:** Geometry of the NREL Phase VI Wind Turbine, figure adopted from [40]

Two pitch angles of  $3^\circ$  and  $-10^\circ$  are studied in this research. The turbine blade is simulated without the wind turbine tower and blade tip plate. The computational domain shown in Fig. 3 is meshed using structured grid with an overall mesh size of 5

million points. Close to the blade, there are 201 points in the chord direction, 85 points in the spanwise and 51 points normal to blade. The mesh size and number of points in each direction are similar to those used by other research groups in [10,41]. The first cell spacing close to blade wall is set to  $1 \times 10^{-5}$  to ensure  $y^+$  close to 1.

As shown in Fig. 3, the computational domain consists of a rotational inner domain (in blue) and a stationary outer domain (in black). The rotational domain is  $3R$  in length and  $2.5R$  in width. The stationary domain has a length of  $6R$  and width of  $8.5R$ . Frozen rotor boundary condition is applied on the interface between rotational and stationary domains with the blade located at zero azimuth. The mesh at the rotational frame and stationary frame are one-to-one connected to ensure flux conservation. The flow variables are converted between the rotational and stationary frames. The boundary conditions of total pressure, total temperature and flow angle are imposed at the upstream inlet boundary of the stationary domain. A static pressure boundary condition is applied at the outlet boundary. Only one blade is simulated with the  $180^\circ$  periodic boundary condition applied on two sides of the hub domain. The convergence criterion is that the L2-norm residual reduced by more than 4 orders of magnitude.

The computational results are validated with the experiment of series S [40] at rotor RPM of 72 at the wind speed ( $U_\infty$ ) of 7m/s, 10m/s, 15m/s, 20m/s and 25m/s with the pitch angle of  $3^\circ$ . Fig. 4 compares the computed power output with the experiments and two other research groups' CFD results [4,42]. The power output is peaked at the wind speed of 10m/s. The computed power output is generally in a good agreement with the experiment except at 7m/s, at which the power is a little over predicted.

The measured surface pressure coefficient distributions at 7m/s, 15m/s and 25m/s are used for comparison with the CFD prediction. The pressure coefficient ( $C_p$ ) of span 30%, 47%, 63% and 95% are presented, which are computed based on Eq. (12), where  $\omega$  is the angular velocity of the wind turbine,  $R$  is the radius at local span,  $p_\infty$  and  $\rho_\infty$  are the freestream static pressure and density.

$$C_p = \frac{P - p_\infty}{0.5 * \rho_\infty (U_\infty^2 + (\omega R)^2)} \quad (12)$$

Fig. 5, Fig. 6 and Fig. 7 show the  $C_p$  comparison between the CFD prediction and the experiment at the four span locations. The agreement is overall very good except at the low span of 30% span for the speed of 15m/s and 25m/s, where the flows are massively separated and the RANS model tends to be inadequate to resolve it. Similar discrepancy is also reported by other researchers [4,43–45]. Overall, the torque and  $C_p$  predicted by the present numerical simulation achieves a good agreement with

the experiment and is thus used as reference to compare the performance of the CFJ wind turbine.

## THE CO-FLOW JET WIND TURBINE

Fig. 8 shows the configuration of 3D CFJ wind turbine that is created based on the optimal configuration of 2D CFJ-S809 airfoil [22] as shown in Fig. 9. The optimal 2D CFJ-S809 airfoil is able to achieve a significant increase of the maximum lift coefficient ( $C_{Lmax}$ ) by 43% and aerodynamic efficiency ( $C_L/C_D$ ) by 175%. For the 3D CFJ wind turbine, the CFJ covers from 26% span to tip. An injection duct (in blue) is constructed at near leading edge at 4%C (chord) oriented tangentially to the local blade surface to ensure a tangential injection of co-flow jet. A suction duct (in red) is implemented near mid-chord at 53%C to suck-in flow and achieves ZNMF flow control. The suction surface is translated downward from 4%C to 53% by 0.1%C to accommodate the tangential injection. The injection outlet slot size is 0.75%C based on the local airfoil chord length and suction slot size is 1.0%C. Since the wind turbine blade shape is tapered, the CFJ slot-size based on the local chord is therefore decreased from the hub to tip.

The power generation is determined by the integral of the local torque multiplied by the angular velocity from the very hub to the very tip of the blade. The torque and thrust force calculation of the CFJ-S809 airfoil at each span considers the jet reactionary force due to CFJ injection and suction effects. Based on the control volume analysis of Zha et al. [46], the expressions for these reactionary forces are given as:

$$F_{z_{cfj}} = (\dot{m}_j V_{j1} + p_{j1} A_{j1}) * \cos(\theta_1 - \alpha) - (\dot{m}_j V_{j2} + p_{j2} A_{j2}) * \cos(\theta_2 + \alpha) \quad (13)$$

$$F_{x_{cfj}} = (\dot{m}_j V_{j1} + p_{j1} A_{j1}) * \sin(\theta_1 - \alpha) + (\dot{m}_j V_{j2} + p_{j2} A_{j2}) * \sin(\theta_2 + \alpha) \quad (14)$$

where the subscripts 1 and 2 stand for the injection and suction respectively, and  $\theta_1$  and  $\theta_2$  are the angles between the injection and suction slot's surface and a line normal to the airfoil chord.  $\alpha$  is the angle of attack.

The torque (tangential) force ( $dF_T$ ), thrust (axial) force ( $d_T$ ) and power ( $dP_W$ ) at the radius  $r$  with the span length  $dr$  are:

$$dP_W = \omega r \cdot dF_T \quad (15)$$

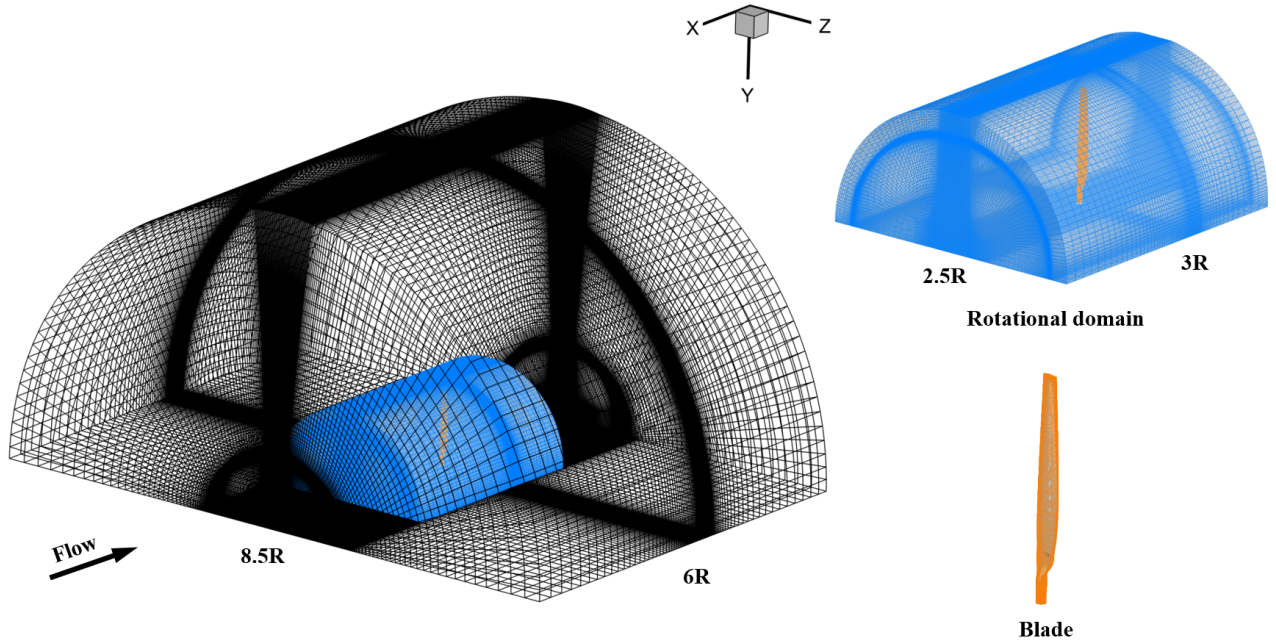


FIGURE 3: Mesh topology

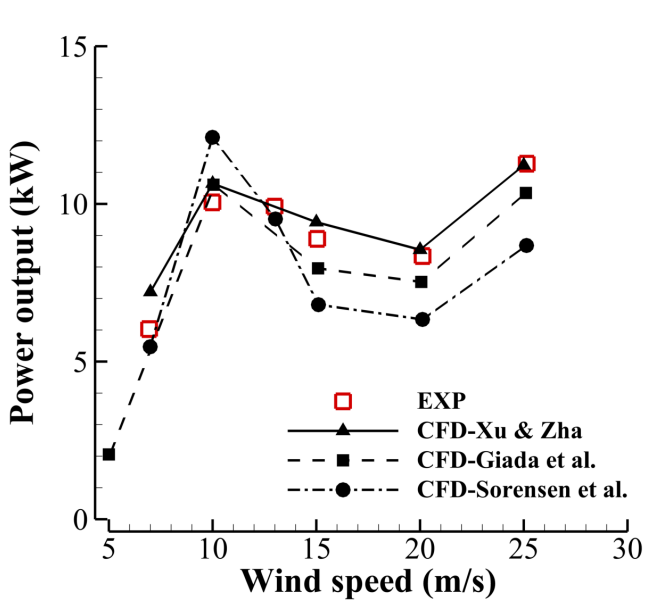


FIGURE 4: Power generation of the baseline wind turbine at various wind speeds, pitch angle of  $3^\circ$

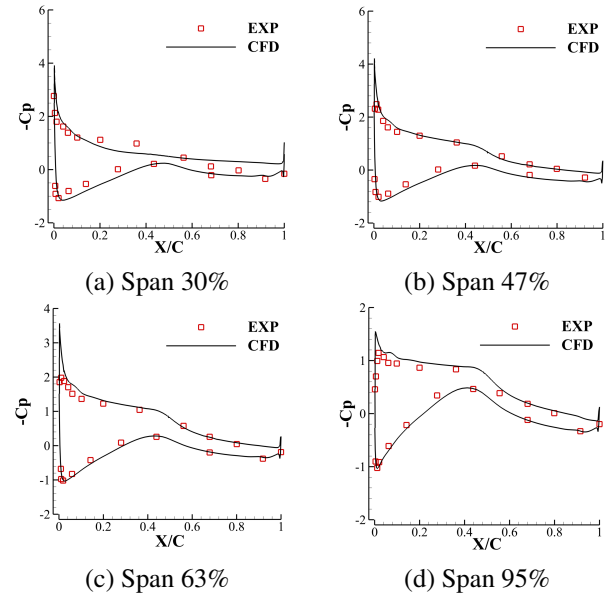


FIGURE 5:  $C_p$  distributions of the wind turbine at wind speed of 7m/s, pitch angle of  $3^\circ$

$$dF_T = (R'_z - F_{z_{cfj}})dr \quad (16)$$

$$dT = (R'_x - F_{x_{cfj}})dr \quad (17)$$

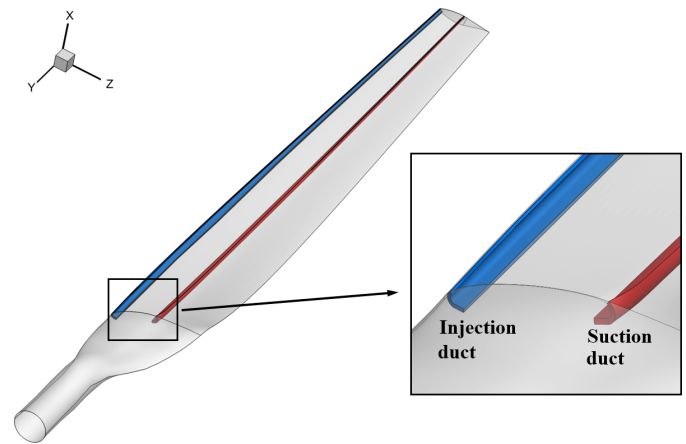
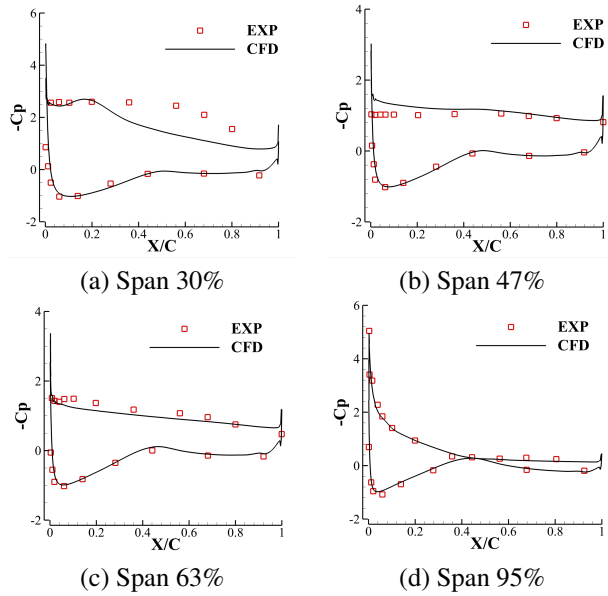


FIGURE 8: Illustration of 3D CFJ wind turbine

FIGURE 6:  $C_p$  distributions of the wind turbine at wind speed of 15m/s, pitch angle of  $3^\circ$

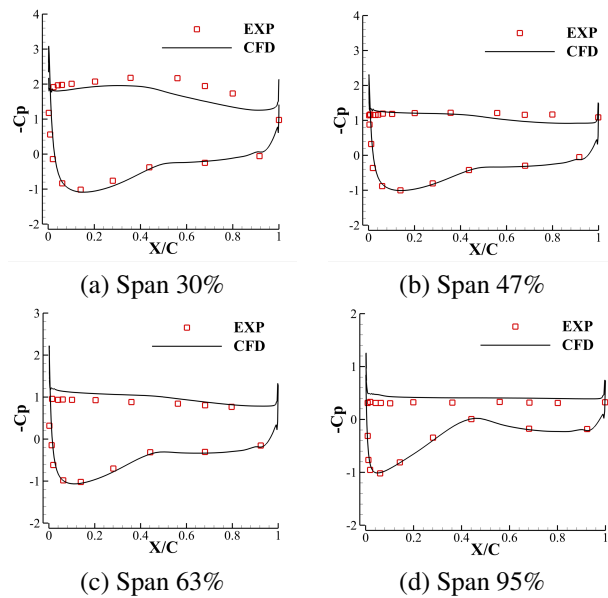


FIGURE 7:  $C_p$  distributions of the wind turbine at wind speed of 25m/s, pitch angle of  $3^\circ$

where  $R'_z$  and  $R'_x$  are the surface integral of pressure and shear stress in  $z$  (tangential) and  $x$  (axial) direction. For CFJ wind turbine simulations, the total thrust and torque are calculated by integrating Eqs.(15) to (17) along the entire span.

The power generation of the baseline wind turbine is com-

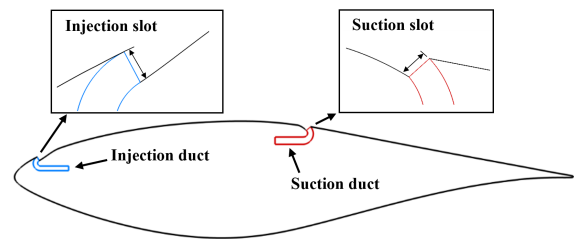


FIGURE 9: The optimal configuration of the 2D CFJ-S809 airfoil [22]

pared with the CFJ wind turbine at the same  $C_\mu$  of 0.06 in Fig. 10 with the pitch angle fixed at  $3^\circ$ . The wind turbine is designed to achieve the optimal efficiency at 7m/s with the tip speed ratio of 5.42 and the pitch angle of  $3^\circ$ . Fig. 10 indicates that the co-flow jet improves the wind turbine power output more at the off-design wind speed. Table. 1 gives the quantitative values of the power improvement at each speed, where  $P_{Wb}$  is the baseline wind turbine power,  $P_{Wc}$  is the power with CFJ applied and  $P_{CFJ}$  is the power consumed by the CFJ active flow control, and  $\bar{V}_j$ ,  $\bar{m}$ ,  $P_c$  are the normalized injection relative velocity, relative mass flow rate of CFJ and power coefficient in the turbine rotating frame. The  $P_{net}$  is the net power generation of the CFJ wind turbine after deducting the CFJ power consumption as expressed in Eq. (18). At the wind speed of 15m/s, the peak  $P_{net}$  is achieved with an increase of 70.2% ( $\Delta P_{net}$ ) compared to the baseline wind turbine due to the reduced flow separation by the CFJ. At the high speed of 25m/s,  $\Delta P_{net}$  improvement percentage decreases because the flow separation is too severe to be suppressed by the low  $C_\mu$  of 0.06. In addition, the CFJ consumes more power when the freestream velocity is increased. At the design speed of 7m/s, the CFJ wind turbine actually decreases

the power output by 10.1%. The reason is that the baseline wind turbine performs very well at the design speed and there is not much room for improvement. Therefore, the CFJ energy expenditure is much higher than the power output improvement, which results in a negative  $\Delta P_{net}$ .

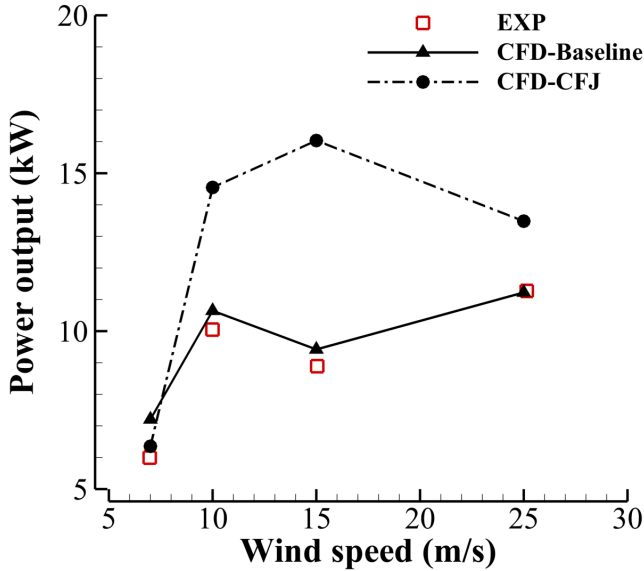


FIGURE 10: Power generation of the baseline and CFJ wind turbine at various wind speed, pitch angle of  $3^\circ$

$$P_{net} = P_{wc} - P_{CFJ} \quad (18)$$

Fig. 11 shows the  $C_p$  comparison of the wind turbine with wind speed of 7m/s. It is clear from the  $C_p$  plots that the surface lift loading is increased and the power generation due to the lift should be increased. However, the CFJ reactionary forces are not shown in the  $C_p$  plots. Fig. 12 gives the torque distribution along the span. It can be seen that the torque due to the CFJ turbine blade surface force is substantially larger than that of the baseline turbine as reflected in Fig. 11. However, after including the CFJ reactionary force described in Eq. (16) and (17), the actual torque is reduced to about the same as that of the baseline as shown in Fig. 12.

Fig. 13 shows the streamlines colored by the Mach number of the baseline and CFJ turbine at 7m/s and pitch angle of  $3^\circ$ . Both have no flow separation with the optimal power output. Fig. 14 is the same plot for the 15m/s with the same  $C_\mu$  and pitch angle. The baseline turbine flow is massively separated. The

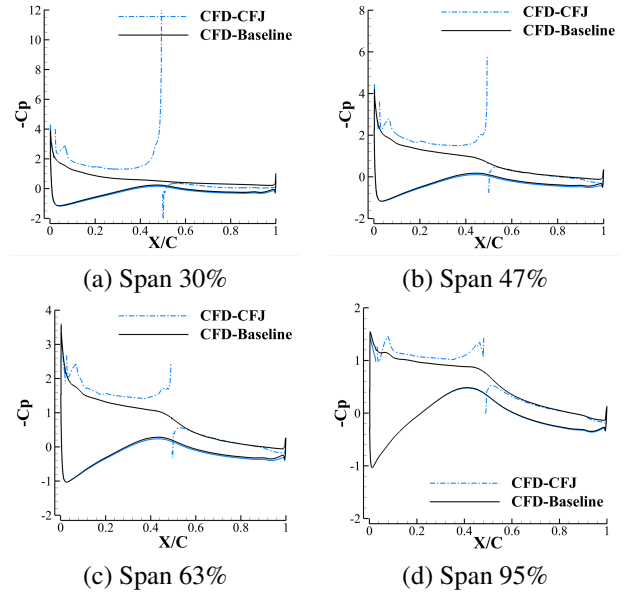


FIGURE 11:  $C_p$  distributions of the baseline and CFJ wind turbine with wind speed of 7m/s, pitch angle of  $3^\circ$

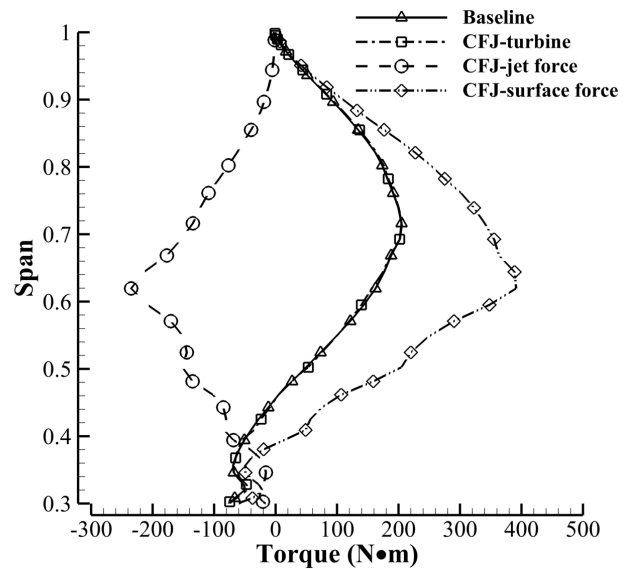


FIGURE 12: Torque distributions along span at 7m/s, pitch angle of  $3^\circ$

CFJ turbine flow separation is reduced, but not completely eliminated. Such a reduced flow separation achieves a power output increase by 70.2% as shown in Table 1.

**TABLE 1:** Performance of the baseline and CFJ wind turbine at pitch angle of 3°

$U_\infty$ (m/s)	Baseline	CFJ								
	$P_{Wb}$ (W)	$C_\mu$	$\bar{V}_j$	$\Gamma$	$\bar{m}$	$P_c$	$P_{Wc}$ (W)	$P_{CFJ}$ (W)	$P_{net}$ (W)	$\Delta P_{net}$
7	7070.2	0.06	1.47	1.008	0.020	0.032	7362.8	1006.8	6356.0	-10.1%
10	11562.5	0.06	1.48	1.006	0.020	0.025	15426.8	876.5	14550.3	25.8%
15	9422.5	0.06	1.51	1.014	0.020	0.050	18173.3	2138.2	16035.1	70.2%
25	11225.4	0.06	1.48	1.027	0.020	0.067	18370.8	4887.5	13483.3	20.1%

### Maximize CFJ Turbine Power Output

The results above show a small improvement of the power output at the design speed of 7m/s at the pitch of 3° and a large improvement for the off design speed. The question is how to maximize the efficiency of the CFJ turbine with its advantage, in particular at a low speed. The proposed strategy is to design the CFJ turbines at a substantially higher angle of attack that conventional turbines would be stalled, whereas the CFJ turbine will generate much higher lift coefficient and ratio of lift to drag, and hence extract more power from the wind flow by removing the flow separation at a low CFJ energy expenditure. We take the example of  $U_\infty=15\text{m/s}$  and 7m/s to demonstrate the new design strategy.

For  $U_\infty=15\text{m/s}$ , Fig. 14 shows that the turbine blades experience a very high angle of attack at pitch angle of 3° that the baseline blade is massively separated. The CFJ turbine blade with the  $C_\mu=0.06$  is not enough to fully remove the flow separation. In the practical operation, the pitch angle would be increased to reduce the blade angle of attack, mitigate the flow separation and achieve stable turbine load for structure protection. For a CFJ turbine, the simple way to remove the flow separation is to increase the CFJ injection jet momentum coefficient to  $C_\mu=0.23$ . As shown in Fig. 15, the flow separation is completely removed and very high suction peak is achieved at the blade surface as shown in Fig. 16. As expected, the power increase achieved by the CFJ turbine is 233.6%.

Fig. 17 shows the power output of the CFJ wind turbine at various  $C_\mu$  from 0 (baseline) to 0.32. The maximum power improvement is 233.6% compared to the baseline, which is achieved with  $C_\mu$  of 0.23. As the  $C_\mu$  continue to increase to 0.32, the power improvement is reduced due to the substantially increased CFJ power consumption that offsets the net improvement.

For the freestream speed at  $U_\infty=7\text{m/s}$ , the baseline turbine design has no flow separation and is at the optimal flow condition. To extract more power from the wind flow by increasing the turbine lift, the pitch angle is reduced by 13° from 3° to -10° to create a 13° higher angle of attack for the turbine. Furthermore, in order to reduce the CFJ power consumption and achieve higher  $P_{net}$ , the injection and suction slot sizes are increased to 1.0%C and 1.3%C. Such method follows the CFJ power reduction prac-

tice in [22], which decreases the total pressure ratio of the CFJ micro-compressor actuator and reaches lower total enthalpy rise. As shown in Fig. 18, the baseline turbine is massively separated, the CFJ turbine is able to attach the flow with the  $C_\mu$  of 0.14. Fig. 19 shows a significant enhanced suction peak near the blade leading edge, which results in an increased lift coefficient and extra power output by 20.3%. Such strategy is expected to achieve more efficiency gain at low off design speed, including to reduce cut-in speed.

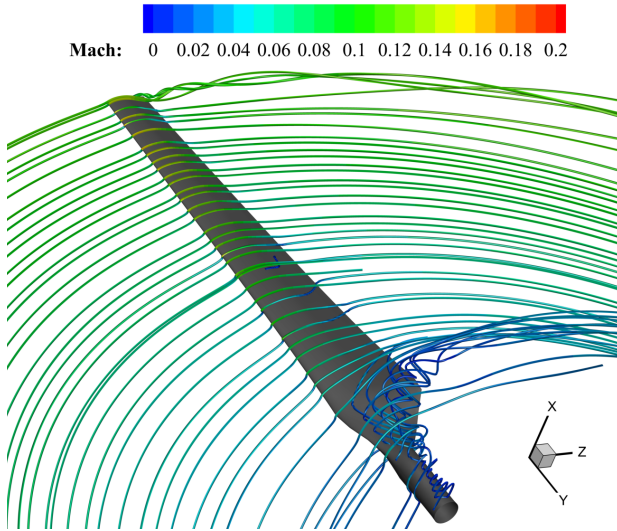
Fig. 20 shows the wake profile of the axial velocity ( $V_x$ ) at 0.5R and 1R location downstream of the turbine blade with wind speed of 7m/s and 15m/s, respectively. There are four cases at 7m/s, two for the pitch angle of 3° (black lines) and two for the pitch angle of -10° (blue lines). The  $C_\mu$  is 0.06 and 0.14 of the CFJ case at 3° and -10° pitch angle respectively. A minor difference is observed between the baseline and CFJ cases at 7m/s with pitch of 3° as shown in the black lines on the left of Fig. 20. This is because the power extraction of the baseline and CFJ wind turbine are about the same at pitch angle of 3°. As pitch angle is reduced to -10°, the baseline wind turbine has a higher wake velocity due to the flow separation that reduces work extraction. The CFJ wind turbine with  $C_\mu$  of 0.14 possesses a significantly lower velocity in wake because it is able to remove flow separation and extract more work from the freestream kinetic energy. For the case at 15m/s, the CFJ wind turbine removes flow separation with a  $C_\mu$  of 0.23, and therefore an obvious difference in  $V_x$  is observed on right of Fig. 20.

Fig. 21 shows the power output of the CFJ wind turbine at 7m/s with various  $C_\mu$  at the pitch angle of -10°. Note that the baseline wind turbine has a negative power output. With CFJ applied, the maximum power output is 8.5 kW at  $C_\mu$  of 0.14, which is 20.3% improvement compared to the baseline wind turbine at the design pitch angle of 3°. This again indicates that CFJ wind turbine is more efficient at high angle of attack operation.

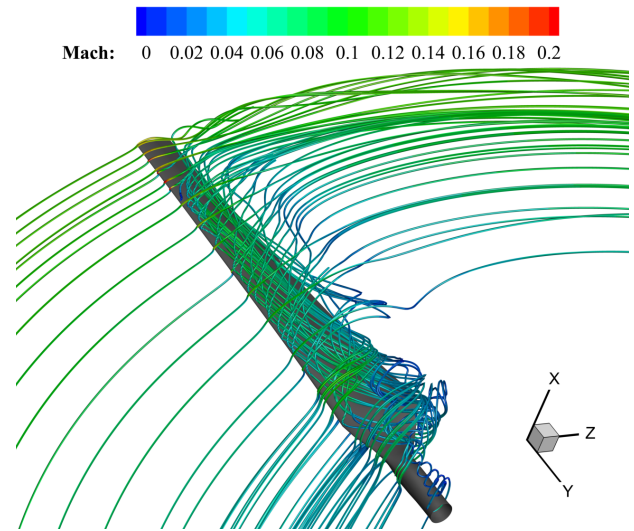
Table 2 compares the optimal CFJ power output at 7 m/s and pitch angle of -10° with the baseline optimal power output at the same speed and pitch angle of 3°. If we see the power output of CFJ wind turbine ( $P_{Wc}$ ), it achieves an efficiency of 63.5% that exceeds the Betz's limit. However, this is because external energy is added to the system by CFJ. The derivation of the Betz's limit is based on the condition that the only energy

**TABLE 2:** CFJ wind turbine cases with the highest power output

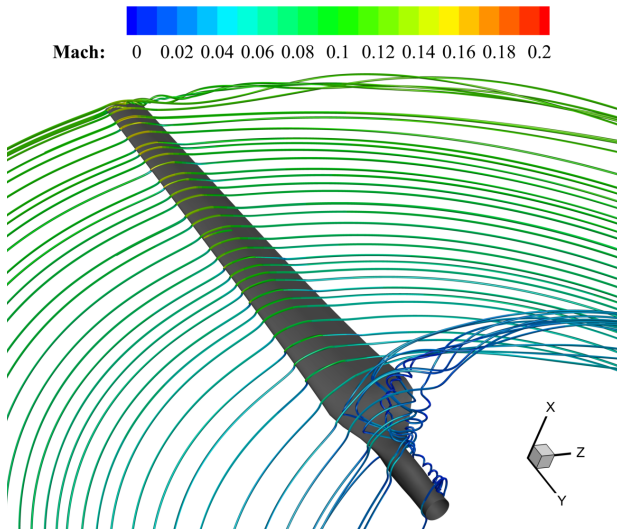
$U_\infty$ (m/s)	Baseline		CFJ									
	Pitch	$P_{Wb}$ (W)	Pitch	$C_\mu$	$\bar{V}_j$	$\Gamma$	$\bar{m}$	$P_c$	$P_{Wc}$ (W)	$P_{CFJ}$ (W)	$P_{net}$ (W)	$\Delta P_{net}$
7	3°	7070.2	-10°	0.14	1.90	1.010	0.036	0.07	10752.0	2249.8	8502.2	20.3%
15	3°	9422.5	3°	0.23	2.93	1.033	0.040	0.23	41161.6	9732.0	31429.6	233.6%



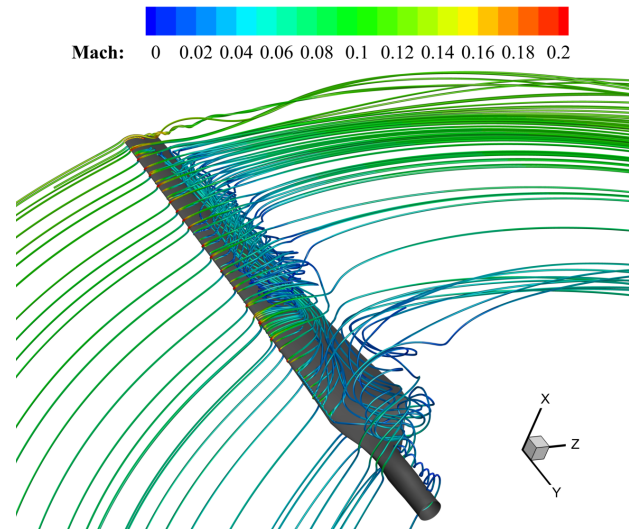
(a) Baseline wind turbine,  $U_\infty=7\text{m/s}$



(a) Baseline wind turbine,  $U_\infty=15\text{m/s}$



(b) CFJ wind turbine,  $U_\infty=7\text{m/s}$ ,  $C_\mu=0.06$



(b) CFJ wind turbine,  $U_\infty=15\text{m/s}$ ,  $C_\mu=0.06$

**FIGURE 13:** Streamlines of the baseline and CFJ wind turbine colored by the relative Mach number, wind speed of 7m/s, pitch angle of 3°

**FIGURE 14:** Streamlines of the baseline and CFJ wind turbine colored by the relative Mach number, wind speed of 15m/s, pitch angle of 3°

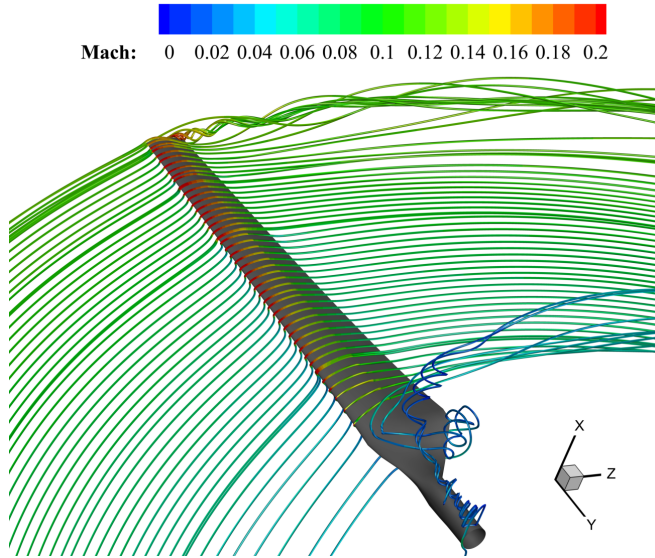


**FIGURE 15:** Streamlines of the CFJ wind turbine colored by the relative Mach number, wind speed of 15m/s,  $C_{\mu}$  of 0.23 and pitch angle of  $3^{\circ}$

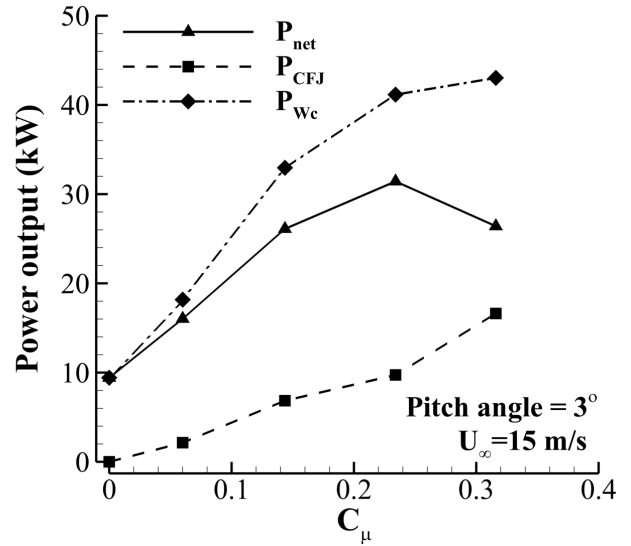


**FIGURE 17:** Power output of the CFJ wind turbine with various  $C_{\mu}$ , wind speed of 15m/s, pitch angle of  $3^{\circ}$

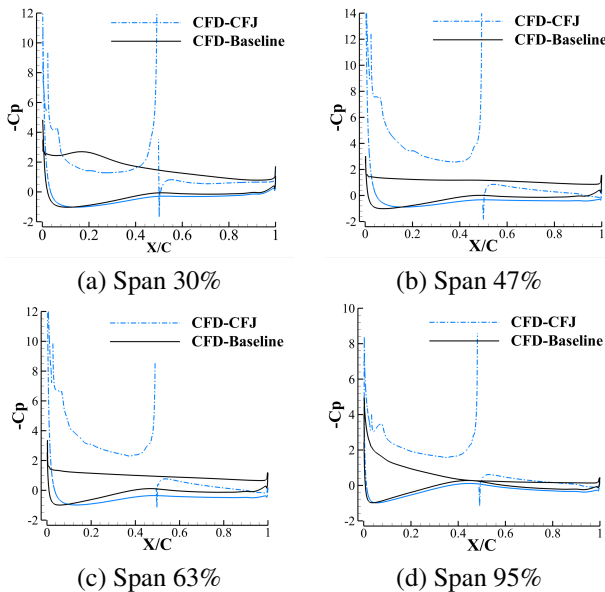


**FIGURE 16:**  $C_p$  distributions of the baseline and CFJ wind turbine with separation removed,  $U_{\infty} = 15$ m/s,  $C_{\mu}$  of 0.23 and pitch angle of  $3^{\circ}$

transfer is from the wind to the turbine and no external energy is added to the system. To acquire the net efficiency for CFJ wind turbine, the CFJ power consumption ( $P_{CFJ}$ ) has to be deducted. For the CFJ wind turbine at 7 m/s with pitch angle of  $-10^{\circ}$ , the

net efficiency is 50.2%.

As indicated in Table 2, the total pressure ratio is very low and far less than 1.1. Such low total pressure ratio is not expected to change much for large wind turbines since it is not sensitive when the Reynolds number is greater than 1 million. In other words, such low total pressure ratio is not unique for the current wind turbine blade but a typical value for the general wind turbine applications. For most wind turbines, the HVAC (Heating, ventilation, and air conditioning) fans or custom designed fans could be used for CFJ. An efficiency of 90% for this type of fans is very achievable today. Taking an averaged CFJ fan efficiency of 80%, the realistic power output improvement at freestream speed of 7 m/s is 12.3%. For the 15 m/s, the power output improvement is 207.7%.

## CHALLENGES WITH CFJ WIND TURBINES

Even though the CFJ wind turbine appears to be promising to improve the wind turbine power output across a range of wind speeds, it brings challenges that do not exist for conventional turbines. Some of the challenges may have straightforward solutions, some may need more efforts. For example, how to strengthen the structures of the blades when there are slots opened along the blade span? How to control the compressors embedded inside the blade with sensors? How to minimize the cost of the added compressors to reduce the overall cost per unit power generated? All these questions are important to make the CFJ turbines for practical use. However, they are beyond the scope of the present paper and will be left for future study.

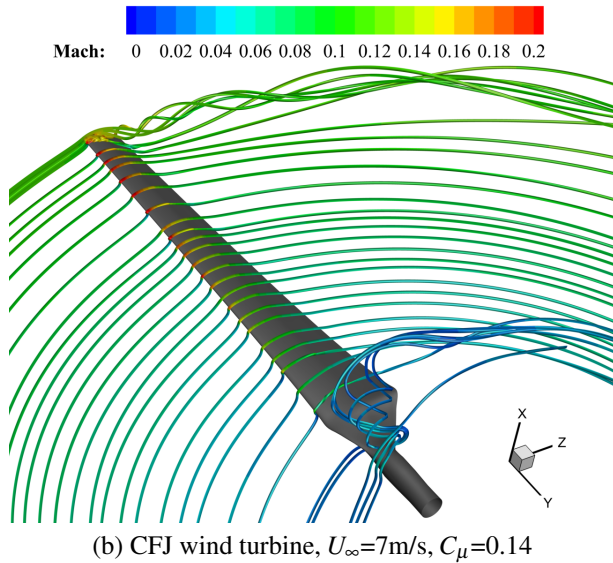
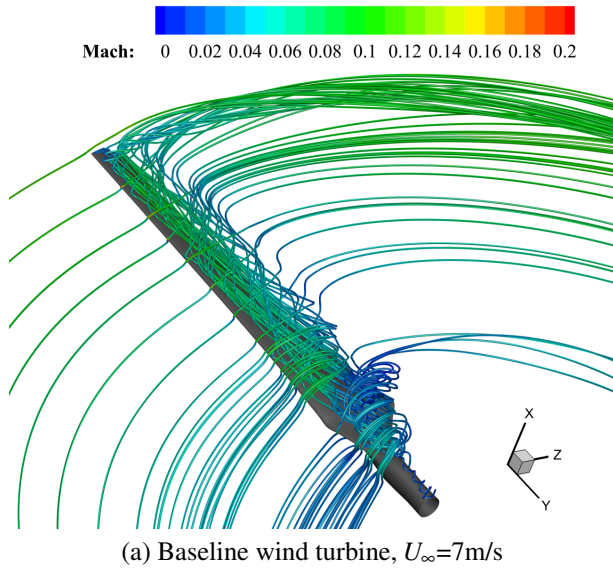


**FIGURE 18:** Streamlines of the baseline and CFJ wind turbine colored by the relative Mach number, wind speed of 7m/s, pitch angle of  $-10^\circ$

## CONCLUSIONS

This paper applies Co-flow Jet (CFJ) active flow control airfoil to a NREL horizontal axis wind turbine for power output improvement. CFJ is a zero-net-mass-flux active flow control method that dramatically increases airfoil lift coefficient and suppresses flow separation at a low energy expenditure. The 3D Reynolds Averaged Navier-Stokes (RANS) equations with one-equation Spalart-Allmaras (SA) turbulence model are solved to simulate the 3D flows of the wind turbines. The baseline wind turbine is the NREL 10.06m diameter phase VI wind turbine and

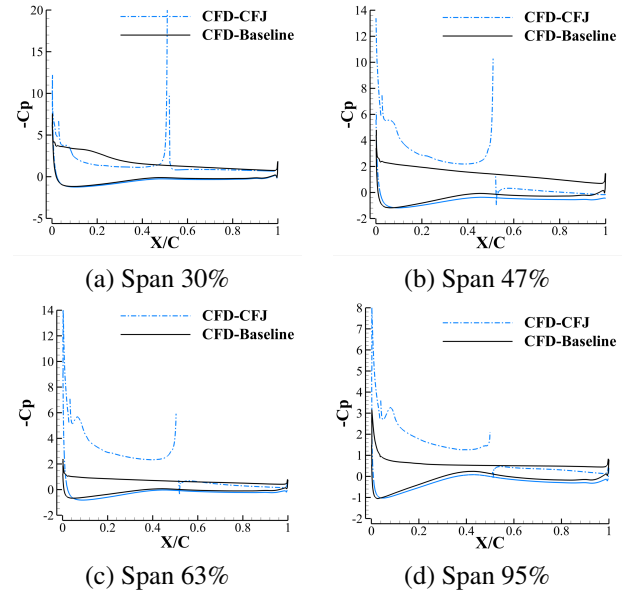


**FIGURE 19:**  $C_p$  distributions of the baseline and CFJ wind turbine with separation removed,  $U_\infty = 7\text{m/s}$ , pitch angle =  $-10^\circ$

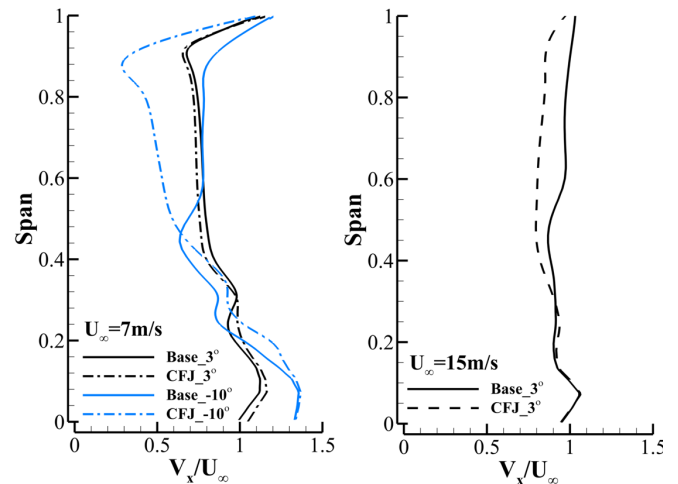


**FIGURE 20:** Spanwise distribution of  $V_x$  at the downstream of the blade

is modified to a CFJ blade by implementing CFJ along the span. The baseline wind turbine performance is validated with the experiment at three wind speeds, 7m/s, 15m/s, and 25m/s. The predicted blade surface pressure distributions and power output agree well with the experimental measurements. The study indicates that the CFJ can enhance the power output at the condition where angle of attack is increased to the level that conventional wind turbine is stalled. At the speed of 7m/s that the NREL turbine is designed to achieve the optimum efficiency at

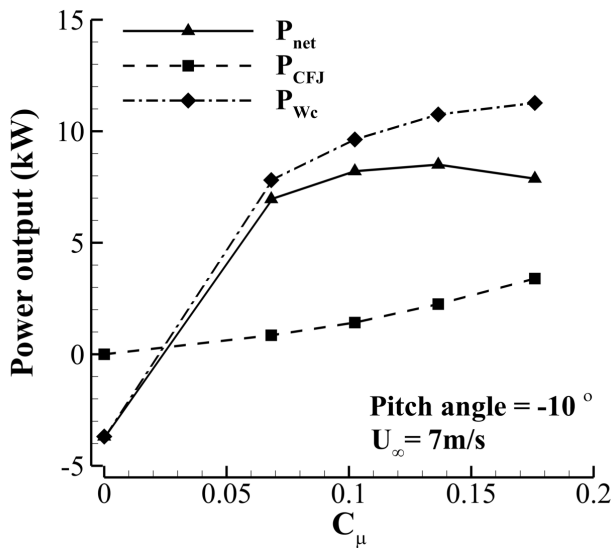


**FIGURE 21:** Power output of the CFJ wind turbine with various  $C_\mu$ , wind speed of 7m/s, pitch angle of  $-10^\circ$

the pitch angle of  $3^\circ$ , the CFJ turbine does not improve power output. When the pitch angle is reduced by  $13^\circ$  to  $-10^\circ$ , the baseline wind turbine is stalled and generates negative power output at 7m/s. But the CFJ wind turbine increases the power output by 12.3% assuming CFJ fan efficiency of 80%. This is an effective method to extract more power from the wind at all speeds. It is particularly useful at low speeds to decrease cut-in speed and increase power output without exceeding the structure limit. At the freestream velocity of 15m/s and the CFJ momentum coefficient  $C_\mu$  of 0.23, the net power output is increased by 207.7% assuming the CFJ fan efficiency of 80%, compared to the baseline wind turbine due to the removal of flow separation. The CFJ wind turbine appears to open a door to a new area of wind turbine efficiency improvement and adaptive control for optimal loading.

## ACKNOWLEDGMENT

The authors would like to acknowledge the computing resource provided by the Center for Computational Sciences at the University of Miami. The authors would also like to thank Dr. Yan Ren for his help and support for this research.

Disclosure: The University of Miami and Dr. Gecheng Zha may receive royalties for future commercialization of the intellectual property used in this study. The University of Miami is also equity owner in CoFlow Jet, LLC, licensee of the intellectual property used in this study.

## REFERENCES

- [1] Huang, G.-Y., Shiah, Y., Bai, C.-J., and Chong, W., 2015. "Experimental study of the protuberance effect on the blade performance of a small horizontal axis wind turbine". *Journal of Wind Engineering and Industrial Aerodynamics*, **147**, pp. 202–211.
- [2] Bai, C.-J., Wang, W.-C., and Chen, P.-W., 2016. "The effects of sinusoidal leading edge of turbine blades on the power coefficient of horizontal-axis wind turbine (hawt)". *International journal of green energy*, **13**(12), pp. 1193–1200.
- [3] Zhang, R.-K., and Wu, V. D. J.-Z., 2012. "Aerodynamic characteristics of wind turbine blades with a sinusoidal leading edge". *Wind Energy*, **15**(3), pp. 407–424.
- [4] Abate, G., and Mavris, D. N., AIAA 2017-4626. "Cfd analysis of leading edge tubercle effects on wind turbine performance". In 15th international energy conversion engineering conference, p. 4626.
- [5] Mueller-Vahl, H., Pechlivanoglou, G., Nayeri, C., and Paschereit, C., 2012. "Vortex generators for wind turbine blades: A combined wind tunnel and wind turbine parametric study". In Turbo Expo: Power for Land, Sea, and Air, GT2012-69197, Vol. 44724, American Society of Mechanical Engineers, pp. 899–914.
- [6] Wang, H., Zhang, B., Qiu, Q., and Xu, X., 2017. "Flow control on the nrel s809 wind turbine airfoil using vortex generators". *Energy*, **118**, pp. 1210–1221.
- [7] Gao, L., Zhang, H., Liu, Y., and Han, S., 2015. "Effects of vortex generators on a blunt trailing-edge airfoil for wind turbines". *Renewable Energy*, **76**, pp. 303–311.
- [8] Shun, S., and Ahmed, N., 2012. "Wind turbine performance improvements using active flow control techniques". *Procedia engineering*, **49**, pp. 83–91.
- [9] Cerretelli, C., Wuerz, W., and Gharaibah, E., 2010. "Unsteady separation control on wind turbine blades using fluidic oscillators". *AIAA journal*, **48**(7), pp. 1302–1311.
- [10] Tran, S. A., Corson, D. A., and Sahni, O., 2014. "Synthetic jet based active flow control of dynamic stall phenomenon on wind turbines under yaw misalignment". In 32nd ASME Wind Energy Symposium, p. 0871.
- [11] Zhu, H., Hao, W., Li, C., and Ding, Q., 2018. "Simulation on flow control strategy of synthetic jet in an vertical axis wind turbine". *Aerospace Science and Technology*, **77**, pp. 439–448.
- [12] Maldonado, V., Boucher, M., Ostman, R., and Amitay, M., 2009. "Active vibration control of a wind turbine blade using synthetic jets.". *International Journal of Flow Control*, **1**(4).
- [13] Yen, J., and Ahmed, N. A., 2013. "Enhancing vertical axis wind turbine by dynamic stall control using synthetic jets". *Journal of Wind Engineering and Industrial Aerodynamics*, **114**, pp. 12–17.

- [14] Zha, G.-C., F Carroll, B., Paxton, C. D., Conley, C. A., and Wells, A., 2007. "High-performance airfoil using coflow jet flow control". *AIAA journal*, **45**(8), pp. 2087–2090.
- [15] Lefebvre, A., Dano, B., Bartow, W., Fronzo, M., and Zha, G., 2016. "Performance and energy expenditure of coflow jet airfoil with variation of mach number". *Journal of Aircraft*, **53**(6), pp. 1757–1767.
- [16] G. Zha, W. Gao, and C.D. Paxton, 2007. "Jet Effects on Co-Flow Jet Airfoil Performance". *AIAA Journal*, **45**, pp. 1222–1231.
- [17] G.-C. Zha, C. Paxton, A. Conley, A. Wells, and B. Carroll, 2006. "Effect of Injection Slot Size on High Performance Co-Flow Jet Airfoil". *AIAA Journal of Aircraft*, **43**, pp. 987–995.
- [18] Yang, Yunchao and Zha, Gecheng, AIAA 2017-1693. "Super-Lift Coefficient of Active Flow Control Airfoil: What is the Limit?". *AIAA SCITECH2017, 55th AIAA Aerospace Science Meeting, Grapevine, Texas*.
- [19] Zhang, J., Xu, K., Yang, Y., Ren, Y., Patel, P., and Zha, G., June 25-29, 2018. Aircraft control surfaces using co-flow jet active flow control airfoil. AIAA Paper 2018-3067, 2018 Applied Aerodynamics Conference, Atlanta, Georgia.
- [20] Xu, K., Zhang, J., and Zha, G., 7-11 January 2019. Drag minimization of co-flow jet control surfaces at cruise conditions. AIAA 2019-1848, AIAA Scitech 2019 Forum, San Diego, California.
- [21] Lefebvre, A., and Zha, G., 2013. "Numerical simulation of pitching airfoil performance enhancement using co-flow jet flow control".
- [22] Xu, K., and Zha, G., 15-19 June, 2020. Investigation of coflow jet active flow control for wind turbine airfoil. AIAA Paper will be virtually presented in 2020 AIAA AVIATION Forum and Exposition, AIAA 2020-2942.
- [23] Lefebvre, A. and Dano, B. and Bartow, W. and Di Franzo, M. and Zha, G.-C., 2016. Performance and Energy Expenditure of Coflow Jet Airfoil with Variation of Mach Number. AIAA Paper 2013-0490, AIAA Journal of Aircraft, DOI: 10.2514/1.C033113.
- [24] Spalart, P., and Allmaras, S., 06 January 1992 - 09 January 1992. A One-equation Turbulence Model for Aerodynamic Flows. AIAA-92-0439, 30th Aerospace Sciences Meeting and Exhibit, Reno, NV, U.S.A.
- [25] Wang, B.-Y., Haddoukessouni, B., Levy, J., and Zha, G.-C., 2007. Numerical Investigations of Injection Slot Size Effect on the Performance of Co-Flow Jet Airfoil. AIAA Paper 2007-4427.
- [26] Shen, Y.-Q., Zha, G.-C., and Wang, B.-Y., 2009. "Improvement of Stability and Accuracy of Implicit WENO Scheme". *AIAA Journal*, **47**, pp. 331–344.
- [27] Shen, Y.-Q. and Zha, G.-C. and Chen, X.-Y., 2009. "High Order Conservative Differencing for Viscous Terms and the Application to Vortex-Induced Vibration Flows". *Journal of Computational Physics*, **228**(2), pp. 8283–8300.
- [28] Shen, Y.-Q. and Zha, G.-C., 2009. "Improvement of the WENO Scheme Smoothness Estimator". *International Journal for Numerical Methods in Fluids*, DOI:10.1002/flid.2186.
- [29] Zha, G.-C., and Bilgen, E., 1996. "Numerical study of three-dimensional flows using unfactored upwind-relaxation sweeping algorithm". *Journal of Computational Physics*, **125**(2), pp. 425–433.
- [30] Wang, B., Hu, Z., and Zha, G.-C., 2008. "General sub-domain boundary mapping procedure for structured grid implicit cfd parallel computation". *Journal of Aerospace Computing, Information, and Communication*, **5**(11), pp. 425–447.
- [31] Wang, B., Haddoukessouni, B., Levy, J., and Zha, G.-C., 2008. "Numerical investigations of injection-slot-size effect on the performance of coflow jet airfoils". *Journal of Aircraft*, **45**(6), pp. 2084–2091.
- [32] Lefebvre, A. and Zha, G.-C., 5-9 Jan 2015. Design of High Wing Loading Compact Electric Airplane Utilizing Co-Flow Jet Flow Control. AIAA Paper 2015-0772, AIAA SciTech2015: 53rd Aerospace Sciences Meeting, Kissimmee, FL.
- [33] Liu, Z.-X. and Zha, G.-C., June 13-17 2016. Transonic Airfoil Performance Enhancement Using Co-Flow Jet Active Flow Control. AIAA Paper 2016-3066, AIAA Aviation, Washington, D.C.
- [34] Lefebvre, A. and Zha, G.-C., 4-8 January 2016. Trade Study of 3D Co-Flow Jet Wing for Cruise Performance. AIAA Paper 2016-0570, AIAA SCITECH2016, AIAA Aerospace Science Meeting, San Diego, CA.
- [35] Wang, B., and Zha, G.-C., 2011. "Detached-eddy simulation of a coflow jet airfoil at high angle of attack". *Journal of aircraft*, **48**(5), pp. 1495–1502.
- [36] Yang, Y., and Zha, G., January 9-13 2017. Super-lift coefficient of active flow control airfoil: What is the limit? AIAA Paper 2017-1693, AIAA SCITECH2017, 55th AIAA Aerospace Science Meeting, Grapevine.
- [37] Im, H.-S. and Zha, G.-C. and Dano, B. P. E., 2014. "Large Eddy Simulation of Coflow Jet Airfoil at High Angle of Attack". *Journal of Fluid Engineering*, vol. 136(2), p. 021101.
- [38] Espinal, D., Im, H.-S., and Zha, G.-C., 2018. "Full-annulus simulation of nonsynchronous blade vibration excitation of an axial compressor". *Journal of Turbomachinery*, **140**(3).
- [39] Iim, H., Chen, X.-Y., and Zha, G., 2012. "Detached-eddy simulation of rotating stall inception for a full-annulus transonic rotor". *Journal of Propulsion and Power*, **28**(4), pp. 782–798.
- [40] Simms, D., Schreck, S., Hand, M., and Fingersh, L. J., 2001. Nrel unsteady aerodynamics experiment in the nasa-ames wind tunnel: a comparison of predictions to measurements. Tech. rep., National Renewable Energy Lab.,

Golden, CO (US).

- [41] Pape, A. L., and Lecanu, J., 2004. “3d navier–stokes computations of a stall-regulated wind turbine”. *Wind Energy: An International Journal for Progress and Applications in Wind Power Conversion Technology*, **7**(4), pp. 309–324.
- [42] Sørensen, N. N., Michelsen, J., and Schreck, S., 2002. “Navier–stokes predictions of the nrel phase vi rotor in the nasa ames 80 ft × 120 ft wind tunnel”. *Wind Energy: An International Journal for Progress and Applications in Wind Power Conversion Technology*, **5**(2-3), pp. 151–169.
- [43] Mo, J.-O., and Lee, Y.-H., 2012. “Cfd investigation on the aerodynamic characteristics of a small-sized wind turbine of nrel phase vi operating with a stall-regulated method”. *Journal of mechanical science and technology*, **26**(1), pp. 81–92.
- [44] Yelmule, M. M., and Vsj, E. A., 2013. “Cfd predictions of nrel phase vi rotor experiments in nasa/ames wind tunnel”. *International Journal of Renewable Energy Research (IJRER)*, **3**(2), pp. 261–269.
- [45] Anjuri, E. V., 2012. “Comparison of experimental results with cfd for nrel phase vi rotor with tip plate”. *International Journal of Renewable Energy Research (IJRER)*, **2**(4), pp. 556–563.
- [46] Zha, G.-C., Gao, W., and Paxton, C., 2007. “Jet Effects on Co-Flow Jet Airfoil Performance”. *AIAA Journal*, No. 6., **45**, pp. 1222–1231.